High performance SERS platforms via parametric optimization of the laser-assisted photodeposition of silver and gold nanoparticles

Hoffmann, Manuel; Wackerow, Stefan; Abdolvand, Amin; Zolotovskaya, Svetlana A.

Published in:
Optical Materials Express

DOI:
10.1364/OME.437900

Publication date:
2021

Research Article | Vol. 11, No. 9 / 1 Sep 2021 / Optical Materials Express 3079

Optical Materials EXPRESS

High performance SERS platforms via parametric optimization of the laser-assisted photodeposition of silver and gold nanoparticles

MANUEL HOFFMANN, STEFAN WACKEROW, AMIN ABDOLVAND, AND SVETLANA A. ZOLOTOVSKAYA*

Materials Science and Engineering Research Cluster, School of Science and Engineering, University of Dundee, Dundee DD1 4HN, United Kingdom
sazolotovskaya@dundee.ac.uk

Abstract: Parametric optimization of the laser-assisted photocatalytic growth of Ag and Au nanoparticles for high SERS enhancement factor performance informed by design of experiment is demonstrated. The photodeposition process was divided into two phases –seeding and growth– in order to achieve the highest possible nanoparticle surface coverage for the size range from 10 to 100 nm. A substantial difference in the parameter effects between the Ag and Au seeding and growth was found. The SERS performance of the photodeposited Ag and Au nanostructures was evaluated at 532, 633 and 785 nm with thiophenol as a probe molecule. A high-enhancement broadband SERS operation was attained with Ag nanostructure grown at high laser fluences. The SERS enhancement factors of 10^5 were achieved with both Ag and Au nanostructures.

1. Introduction

Surface-Enhanced Raman Scattering (SERS) is an extremely powerful optical detection platform for the development of sensitive and quantitative analytical methods suitable for real-time monitoring. This technique provides information about the vibronic 'fingerprint' of a molecule located close to plasmonic nanostructures and therefore allows for a unique classification of the type of analyte detected. This method has also been proven to have a single-molecule detection capability [1,2]. SERS-based approaches have enabled a number of important applications in bioanalytical sensing [3] such as in-vivo tumor targeting [4], glucose sensing at clinically relevant concentrations [5] and microbial system analysis [6], and are considered a major prerequisite for progress in areas such as nanobiotechnology and personalized medicine. Despite the apparent advantages over commonly used fluorescence-based methods, SERS is yet to be established as an analytical tool. In part, this is due to the fact that small variations in the SERS substrate, i.e. preparation, aggregation, surface morphology, etc., have drastic effects on the SERS performance. Therefore, the stability and reproducibility issues of SERS-active substrates have to be addressed in order to facilitate its application in quantitative analysis. Current fabrication techniques of SERS substrates with moderate to high enhancement factors, and reproducible and uniform responses are dominated by e-beam lithography, nanoimprint, self-assembled nanosphere, hybrid nanoporous lithography methods, etc. [7–9]. However, these techniques are still costly and rather cumbersome to produce large area SERS substrates, elevating the price of commercially available SERS platforms.

The applicability of photocatalytic deposition method to production of SERS substrates was first demonstrated using porous SiO_2 monolith containing gold nanoparticles (NPs) formed in volume of the gel upon irradiation with ultraviolet (UV) light [10]. This showed systematic

#437900 https://doi.org/10.1364/OME.437900
Journal © 2021 Received 14 Jul 2021; revised 5 Aug 2021; accepted 12 Aug 2021; published 23 Aug 2021

Optical Materials EXPRESS

and simple approach to control of the particle size and spatial distribution by adjusting the irradiation time and light source type (i.e. laser or lamp). The renewed interest in this production method for SERS applications [11–26] has been supported by the ongoing developments in the field of titanium dioxide (TiO_2) – based photocatalysts for water splitting, organic compounds decomposition, air purification, etc. [27,28]. TiO_2 is a nontoxic semiconductor with a wide bandgap of ~3.2 eV that allows photocatalytic deposition of a variety of noble metals without photocorrosion observed in other semiconductors such as ZnO and CdS [28]. Besides the inherent simplicity and scalability of the photodeposition method, the TiO_2-based nanocomposite SERS substrates benefit further from the SERS performance enhancement owing to the charge transfer by the semiconductor [13,14], and are recognized as renewable under UV irradiation [14–17]. The reported nanoarchitecture optimization strategies for the nanocomposite SERS substrates on TiO_2 thin films, using coherent and incoherent light sources, are predominantly focused on the effects of the precursor concentration [13,14], illumination time and power [11,16,18,29]. Although the NP growth dynamics during photodeposition is well understood [30,31], the results of these studies vary significantly in terms of the mean particle size and SERS enhancement. This is due to the fact that small variations in the thin film fabrication process, post processing steps and thin-film substrate material [32,33] have considerable influence on the resulting nanostructure [15,34,35]. Besides, the established optimization routes consider the influence of a single process parameter only, lacking examination of the joint influence of the multiple process parameters. Therefore, in order to harness the full potential of the photodeposition method for SERS applications a more holistic approach to the optimization of nanoarchitecture has to be taken.

Recently in the photocatalysis field, where the photodeposition of noble metal NPs is extensively used to improve photocatalytic efficiency [28], a parametric study on the photodeposition of platinum was undertaken using the orthogonal-array experimental design method according to G. Taguchi [36]. This showed that a comprehensive optimization procedure can be built by monitoring the influence of a full parameter set whilst keeping the sample number low.

Here, we implemented design of experiment approach for the optimization of nanosecond-pulsed laser-assisted photodeposition of metallic Ag and Au on TiO_2 film. This resulted in enhanced control over nanoarchitecture for high performance SERS applications. The parametric optimization was performed to examine single and combined influence of the laser irradiation parameters, precursor and sacrificial reagent concentrations, enabling a definitive choice of the photodeposition process parameters leading to the smallest possible interparticle distance at high particle densities. The TiO_2 thin film properties were optimized specifically to inhibit the NP growth outside the laser illuminated area to enable future integration of this production method into microfluidic devices for rapid multiplexed SERS assays [37].

2. Experimental methods

Film production: TiO_2 thin films used in the photodeposition were synthesized according to a previously reported method for the production of optically transparent films [38]. Briefly, solution for the sol-gel reaction was prepared by mixing 0.625 g of polyethylene glycol ($M_w = 600$, *Alfa Aesar*) and 2.07 mL of diethylene glycol (*Fisher Chemical*) with ethanol ($\geq$ 99.5% pure, *Honeywell*). After 10 min of stirring, 1.69 mL of titanium (IV) isopropoxide (99.995% metal basis, *Alfa Aesar*) were quickly added to the solution, and the mixture was stirred for further 15 min. The resulting sol was degassed for 20 min, flushed with nitrogen (N_2) and sealed. Borosilicate glass (Ø22 × 0.21 mm^2, D263, *Schott*) was used as a substrate for the thin film deposition in order to alleviate effect of sodium (Na^+) doping on the photocatalytic activity of the resulting films [33]. Before the film deposition substrates were cleaned with acetone, methanol and dried with N_2. A sequential spin-coating deposition at 2500 rpm for 30 s was used to achieve the desired film thickness. For each step 75 µL of the sol-gel were pipetted onto the substrate.

Optical Materials EXPRESS

After each coating step, the substrates were dried at 80°C. The amorphous films were transferred into a preheated oven for calcination at 400, 450 and 500 °C for 30 min.

Laser-assisted photodeposition: The Au and Ag precursor solutions were prepared by mixing the appropriate amounts of 10 mM $HAuCl_4$ (99.99% metal basis, *Alfa Aesar*) or 10 mM $AgNO_3$ (>99.9% metal basis, *Alfa Aesar*) stock solutions, double distilled water and methanol (MeOH, >99.8%, *Fisher Chemical*). For the photodeposition, the TiO_2 substrates were placed in a two-part aluminum sample holder with a machined through hole to prevent back reflection. A rubber O-ring, sandwiched between the glass substrate and the upper part of the sample holder assembly, was used to seal the precursor pool. 190 µL of the precursor solution, sufficient to fully cover the open TiO_2 film surface, were used for each photodeposition experiment.

A 355-nm Nd:YVO_4 laser (*Violino, Laservall*) with a maximum average power of 3 W and a pulse length of 10 ns operating at 30 and 50 kHz was utilized for the Au and Ag photodeposition respectively. The laser beam with a Gaussian intensity profile (M^2 ~1.1) was focused onto the glass surface using a flat-field scanning lens system. The laser beam spot size at the focal plane was measured to be 65 µm at the $1/e^2$ intensity level. The energy fluences in the range from 13 to 38 mJ/cm^2 were employed for the Ag and Au deposition. The laser beam was raster scanned over the TiO_2 surface with the precursor solution in place at different speeds. Depending on the number of pulses per spot required, the scanning speed was varied from 0.36 to 10 mm/s using a computer-controlled two-axis scan head system.

Sample characterization: The transmittance and reflectance spectra of the films prior and post photodeposition were measured in the spectral range from 250 to 1100 nm using a *Jasco V-670 UV/VIS/NIR* spectrophotometer equipped with a 60-mm integrating sphere. The TiO_2 film thickness was measured using *Bruker Dektak XT* stylus profiler equipped with a 2-µm stylus.

A *JEOL JSM-7400F* field emission scanning electron microscope (SEM) was used to obtain high magnification images of the sample surfaces after the photodeposition. A center line area of 3.2 µm^2 was imaged at 60000x magnification to allow automatic particle discrimination. The SEM image segmentation was conducted using an open-source software package *ilastik* [39]. The segmentation was followed by binarization and image analysis using *Fiji* [40]. The *Feret* diameters (D_m), mean NP centroid distances (d_m) and normalized volumes per surface area (V_n) were evaluated to estimate the NP density (n_{NP}) and photodeposition rate. The NP volume was calculated assuming a hemispherical shape with the diameter corresponding to a circle of equal projection of the measured area. These results were normalized to the largest value achieved in the experiment. The number of NP per image used in the analysis ranged from ~220 to ~3400 NPs from the lowest to highest observed densities.

The phase composition of the resulting TiO_2 films was examined using an in-house built Raman microprobe system, equipped with a continuous wave laser source emitting at 633 nm and *Oriel MS257* monochromator fitted with *Andor Newton EMCCD* detector, TE cooled to -70°C. The backscattering configuration was used for the signal collection. The incident power on the samples was 8.05 mW. The Raman spectra were recorded using a 40x objective (*Plan Fluor*, *Nikon*), an accumulation time of 1 s with a total of 10 accumulations, a slit width of 50 µm and a 1200 lines/mm grating.

The SERS performance evaluation was conducted at 532, 633 and 785 nm excitation wavelengths (λ_{exc}). The upright microprobe system described above was used for the measurements at 532 and 633 nm. A purpose-built Raman imaging system based on *Nikon Eclipse Ti-U* inverted microscope equipped with an XYZ nanopositioning stage (*Physik Instrumente*) was used for the measurements and surface mapping at λ_{exc} = 785 nm utilizing a single frequency MOPA system (*Innovative Photonic Solution*). *Andor Shamrock 500i* imaging spectrometer fitted with the *Andor Newton CCD* was employed for the signal acquisition. Here, a 600 lines/mm diffraction grating was used. The slit widths for the SERS evaluation were 100, 150 and 200 µm for 532-, 633- and 785-nm excitation respectively, allowing for >90% of the SERS signal collection in both

Optical Materials EXPRESS

systems. The objective magnification, exposure time and incident power were selected to achieve the highest signal-to-noise ratio and to mitigate photochemical damage to the analyte and SERS substrate. The 40x and 60x Plan Fluor objectives (*Nikon*) with the maximum exposure time of 10 s were used. The maximum incident power measured at the back aperture of the objective was 0.25, 1.5 and 10 mW for $\lambda_{exc} = 532$ nm, 633 nm and 785 nm respectively. The acquired Raman and SERS spectra were post processed to remove the background signal, originating from the glass substrate, by applying a fully automated model-free baseline correction method [41].

Thiophenol (≥ 99%, *Sigma Aldrich*) was chosen as an analyte compound for the SERS enhancement study due to its selective binding affinity to metal surfaces [42]. Self-assembled monolayers (SAM) of thiophenol on the Ag and Au NPs were achieved by soaking the substrates in a 5-mM ethanolic solution for 1 and 2 h respectively [42,43]. The substrates were then rinsed with ethanol for 90 s and left to dry in air before the measurements. At least 21 SERS spectra were taken from each sample with a 10-µm displacement between each measurement point.

The SERS enhancement factor (EF) was calculated according to [44]:

$$EF = \frac{I_{SERS}/N_{surf}}{I_{RS}/N_{vol}} \tag{1}$$

as the intensity ratio between SERS (I_{SERS}) and normal Raman (I_{RS}) scattering normalized by the respective number of analyte molecules N_{surf} and N_{vol}, probed using the 1076 cm^{-1} band of thiophenol. The normal Raman spectrum was measured on pure thiophenol, contained within a cell with a defined height of 70 µm. For all combinations of λ_{exc}/objective magnification, the number of molecules in the normal Raman scattering measurement (N_{vol}) was found from the measurements of the effective scattering hight H_{eff} and area A_{eff} as $N_{vol} = H_{eff} \times A_{eff} \times c_{RS}$ [44]. The number of molecules per unit volume (c_{RS}) was assumed to be 5.86×10^{21} 1/mL. In the SERS experiment, the number of excited molecules per unit area ($N_{surf} = \mu_s \times \mu_M \times A_M \times A_{eff}$) was calculated based on the NP surface areas (μ_s) and densities (μ_M), retrieved from the SEM images the photodeposits, assuming hemispherical NP shape profile. The highest reported SAM packing density (A_M) of 6.8×10^{14} molecules/cm^2 was utilized, allowing for a conservative estimate of the EF substrate performance [45]. The background corrected peak signal intensities were used in the EF calculations.

Photodeposition process optimization: A parametric optimization of the laser-assisted photodeposition process was conducted to achieve the highest possible SERS EF in the visible and near-infrared spectral regions. An average value of SERS EF for Ag- and Au-based SERS substrates is around 10^6, but the localized enhancement may reach peaks of 10^{10}–10^{11} at certain sub-wavelength regions of the nanostructure, where NPs are in aggregate geometries, supporting plasmon hot spots [46–48]. In accordance with plasmon hybridization and classical electromagnetic theories, the interparticle separation distance required to achieve such large SERS EFs is in the sub-10 nm range [49,50]. Thus, the goal of the parametric optimization was to achieve the highest possible NP density for the NP size ranging from 10 to 100 nm.

The process parameters typically considered for Ag and Au photodeposition are the illumination time and intensity [10,11,16,18–21,29,36,51,52], precursor and sacrificial reagent concentrations [13,14,19,20,35,36,52], precursor solution acidity (pH) [36,53,54], as well as the properties of the semiconductor film [15,34–36]. For the parametric optimization carried out in this work *four* process parameters were selected, namely the precursor and sacrificial reagent concentrations, number of pulses per spot and laser fluence. For the purpose of the experimental design, the chosen parameters were grouped in accordance with their influence on the NP growth dynamics, i.e. the deposition rate, particle density and interparticle distance. The initial parameter screening and published data showed that the optimization towards the highest particle density and smallest interparticle distance require two different sets of the optimization parameters. Thus, the photodeposition experiment was conducted in two stages – the *NP seeding* and *growth*.

Optical Materials EXPRESS

The laser-assisted Ag and Au *NP seeding* dynamics was investigated using the 2^k *full factorial experimental design* [55] which enabled examination of both single and joint effects of the process parameters (i.e. *k-factors*) on the photodeposition rate and particle density at fixed number of pulses per spot. Subsequently, factorial analysis of variance (factorial ANOVA) was employed to confirm the magnitude of the process parameters effects on the photodeposition. The levels and factors, listed in Table 1 (*NP seeding*), were selected after an initial photodeposition parameter screening. The *levels −1* and *1* were chosen to reflect the *k-factor* sets with low and high NP depositions respectively, corresponding to the seeding range from low to high NP density points. The upper density point was chosen so that the influence of static coalescence of NPs [56] and radiation shielding [28] effects on the true factor effects could be negated. A total of *eight* images were analysed for the required experimental runs of the 2^3–factorial experiment. The validity of this experimental design was additionally verified by introduction of a center point (see Table 1, *level 0*) to test the assumption of a unidirectional response of the photodeposition results to the factors in the chosen parameter ranges (e.g. a linear increase in the NP size with increase in the precursor concentration, laser fluence, etc.). The process variance was calculated by the repeat measurements of the centre point. The centre point was measured by analysing *six* and *four* areas of Ag and Au NPs respectively, photodeposited at different locations on the same substrate.

Table 1. Photodeposition parameters used in the NP seeding and growth experiments

NP seeding: *2^3 factorial experiment levels and factors*						
	Levels					
	Ag			**Au**		
k-factors	−1	0[a]	1	−1	0[a]	1
(A) Laser fluence (F_L, mJ/cm^2)	13	23	33	20	28	36
(B) Precursor concentration (C_P, mM)	1	2	3	2	5	8
(C) MeOH concentration (C_S, vol-%)	5	7.5	10	5	12.5	20
Number of pulses per spot (N_L, pulses/spot)	1625			975		
Repetition Rate (kHz)	50			30		
NP growth: *photodeposition growth parameters*						
Laser fluence (F_L, mJ/cm^2)	13	27.5/ 33/ 38		36	20	
Precursor concentration (C_P, mM)	3			2	8	
MeOH concentration (C_S, vol-%)	10			20		
Number of pulses per spot (N_L, pulses/spot)	1625-13047	8784		975 - 8960	975 - 9970	

[a]*Level 0 corresponds to the centre point*

The laser-assisted Ag *NP growth* dynamics was investigated at fixed precursor (C_P) and sacrificial reagent (C_S) concentrations enabling optimization towards the smallest possible interparticle distance for the 10–100 nm NP size range based on variation of the number of pulses per spot (N_L) at two different laser fluence levels (F_L). For the Au *NP growth*, in addition to the above-mentioned parameters, two different precursor concentrations were considered. The parameter sets used in the NP growth study are summarized in Table 1 (*NP growth*). This particular choice of the growth parameters was made to take into account the achieved NP seeding density and the antenna effect, leading to the preferential reduction on the already deposited NP [30,31].

The TiO_2 film properties influencing the photodeposition process were not directly incorporated in the parametric optimization to reduce the number of experimental runs required. Instead, the thin film properties were tailored independently to achieve localized NP deposition to enable

Optical Materials EXPRESS

further SERS performance enhancement via tailoring plasmonic properties of the NP arrays accessible with the laser-assisted nano-/micro-structuring techniques.

3. Results and discussion

Photodeposition localization study: Photodeposition process is based on light-induced electrochemistry with two reactions occurring at the same time: oxidation by photogenerated holes, and reduction involving photogenerated electrons (e^-). To enable photodeposition, the redox potential of the metal to be deposited has to match the energy band structure of the semiconductor. It also has to be accompanied by charge carrier separation and migration in the semiconductor. The latter leads to the diffusion of the photogenerated e^- and particle nucleation away from the illuminated area. The diffusion length of the photogenerated e^- is defined by the square root of the product of the e^- lifetime and the diffusion coefficient. The e^- lifetime is governed by the recombination times and reduction kinetics of the ionic species at the surface [57], whereas the diffusion coefficient is determined by the semiconductor properties. The photogenerated e^- diffusion in polycrystalline semiconductors is commonly characterized by the hopping mechanism, governed by surface trapping as well as interfacial properties between the crystals [58]. A decrease in crystal sizes was shown to slow the e^- transport as a result of increase in the trap densities [59]. An increased ratio of the amorphous phase with a slightly larger bandgap than the crystalline TiO_2 was also suggested to further decrease the e^- diffusion length [60,61]. The crystal sizes and degree of crystallization are known to depend on the crystallization temperatures and time. Thus, the TiO_2 film optimization strategy was based on the variation of the film calcination temperature.

The measured Raman response of the TiO_2 films (see Fig. 1(a)), calcined at 400, 450 and 500 °C for 30 min, confirmed formation of anatase TiO_2 phase at all calcination temperatures as previously found in the similar material systems [32]. The presence of metastable brookite phase was also observed. The increase in crystallinity of the TiO_2 films with the increase in calcination temperature was confirmed by the observed increase in the intensity of anatase bands [62]. The observed formation of the metastable polymorph and increase in the amorphous to anatase phase transition temperature were associated with diffusion of Na^+ ions from the glass substrate into the TiO_2 films [32]. The transmittance measurements of the produced films (Fig. 1(b)) showed a high optical transparency of > 90% in the spectral region from 370 to 1000 nm for all calcination temperatures. The thickness of the produced TiO_2 films was measured to be 200 nm for the films calcined at 450 and 500 °C, and 220 nm for the 400 °C calcination. The indirect optical bandgap values of the TiO_2 films were determined by using the *Tauc* relation [63]. The bandgap was estimated from the *Tauc* plots (see the inset in Fig. 1(b)), based on the published approach accounting for the reflections at the air-film-substrate-air interface [64]. The resulting plots showed presence of two distinct linear regions, associated with the presence of two phases, yielding the bandgap values of ~3.46 eV and ~3.32 eV for the high and low energy regions respectively. The observed bandgap increase, compared with the typically reported values of 3.2 eV [65] for anatase phase, was attributed to Na^+ doping of the TiO_2 films [66,67].

Figure 2 shows the results of the laser-assisted photodeposition localization study of the TiO_2 films. For the study, a 3-mM $AgNO_3$ precursor solution containing 10 vol % of MeOH was irradiated with $F_L = 33$ mJ/cm^2 at 50 kHz, with $N_L = 1625$ pulses/spot. The observed lack of readable features for the logotypes shown in Fig. 2(a) and (b) is due to a considerable Ag NP deposition outside the laser irradiated areas, confirmed by the SEM examination of the areas adjacent to the laser-written lines. In contrast, the TiO_2 films calcined at 400 °C (see Fig. 2(c), (d)-(f)) demonstrate a high degree of localized NP deposition, associated with a reduced diffusion length of the photogenerated e^- due to lower crystallinity of the film. All subsequent photodeposition experiments were conducted with the TiO_2 films calcined at 400 °C.

Photodeposition process optimization — 1. NP seeding: In the NP seeding dynamics study, the photodeposition results were evaluated to establish the influence of the processing parameters

Optical Materials EXPRESS

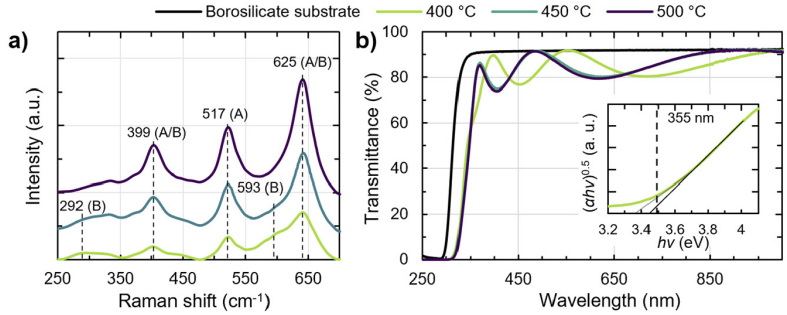

Fig. 1. **(a)** Raman spectra of the TiO_2 films calcined at different temperatures. Anatase (A) and brookite (B) phase peak locations are assigned according to Ref. [68]. **(b)** Transmittance spectra of the produced films with the *Tauc* plot of the film calcined at 400 °C shown in the inset.

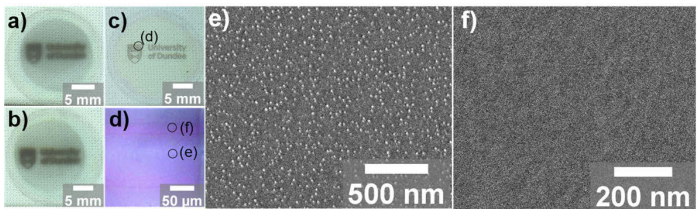

Fig. 2. Laser-assisted photodeposition localization study: Ag NP deposition on the TiO_2 films calcined at **(a)** 500 °C, **(b)** 450°C and **(c)** 400 °C; **(d)** A close-up of the Ag deposition on film calcined at 400 °C; **(e)** SEM image of the laser-written line with Ag NP; **(f)** SEM image of the area between the laser-written lines showing no observable NP deposition. The distance between the laser-written lines is 100 µm, the beam spot diameter is 65 µm at the $1/e^2$ intensity level.

(*k-factors*, Table 1: *NP seeding*) on the NP seeding rate and deposition density. These were estimated using the normalized NP volume per unit area (V_n) and NP mean centroid distance (d_m). The results of the 2^3-factorial photodeposition experiment for the Ag and Au NP seeding are summarized in Fig. 3. The main factor influences, shown in Fig. 3(a, b) and Fig. 3(d, e), qualitatively confirm existence of a combined parameter effect influencing the Ag and Au NP seeding dynamics. The analysis of the main factor effects shows that the NP seeding stage is mainly influenced by the laser fluence F_L (A) and ion concentration C_P (B), with only minor contribution from the increase in MeOH concentration C_S (C). This was confirmed by estimation of the percentage contribution of each parameter relative to the total sum of squares, plotted in Fig. 3(c, f). The probability of the parameter contribution calculations, performed using ANOVA, validated the significant influence of F_L (A) and C_P (B) on the Ag and Au NP d_m and V_n with the *p-values* (p) below 0.05, see Fig. 3(c, f). Thus, for the chosen parameter set, the increase in F_L (A) and C_P (B) resulted in increase in the seeding rate for both Ag and Au NPs. These results conform to the photochemical theory for semiconductor-liquid interfaces that predicts an increase in charge transfer with light intensity, which is further dependent on the concentration of the redox couple at the electrolyte side [69]. However, the relatively small impact of the increase in C_S (C) suggests that the NP seeding dynamics is mass transfer limited rather than charge transfer limited, i.e. dominated by the depletion of the reductants at the TiO_2 surface but not the availability of photogenerated e^- for the metal ion reduction [19,57]. This could explain the

Optical Materials EXPRESS

absence of any appreciable combined influence of F_L and C_S (AC) on the deposition, which should result in a noticeable current doubling effect [30,31,57,70]. The observed joined influence of F_L and C_P (AB) can also include contribution from an increase in the ion diffusion due to the laser-induced heating.

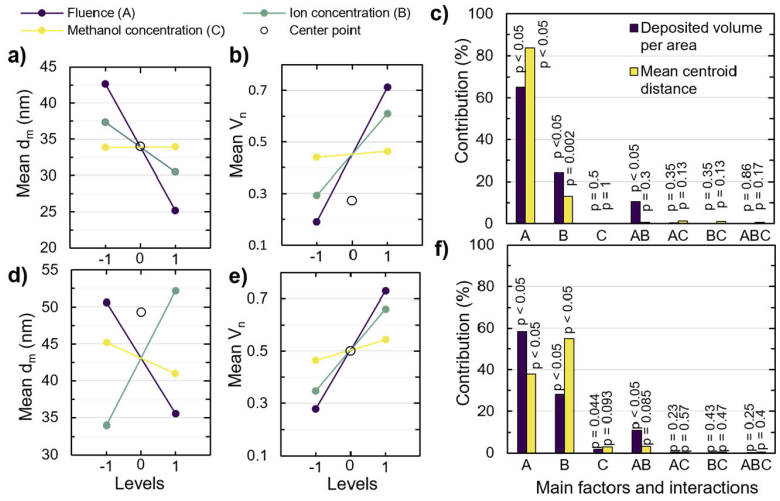

Fig. 3. 2^3 factorial experiments for the laser-assisted Ag (a - c) and Au (d - f) NP seeding stage. The main process parameter (*k-factors*) effects on the mean NP centroid distance (d_m) and normalized NP volume per area (V_n), averaged over all level combinations, for Ag (a, b) and Au (d, e) depositions. Contribution of the process parameters and their interactions, based on the sum of squares, for Ag (c) and Au (f) NP depositions. The significant factor influences ($p < 0.05$) are calculated by ANOVA.

The laser-induced temperature change was estimated in terms of the optical properties of the TiO_2 film, using the method described in Ref. [71]. For the temperature calculations, the specific heat capacity of the film was taken to be equal to the value for mesoporous TiO_2 thin film, adapted from [72]. The mass density of the film was assumed to be 10% lower than the bulk, a typically observed reduction for the spin coated thin films [73]. The film refractive index was retrieved from the transmission spectrum by applying the numerical method described in [74]. For the Ag NP seeding case, the maximum resultant temperature change at the surface of the film in the centre of the gaussian beam after one pulse was estimated to be 41 K for $F_L = 13$ mJ/cm^2 and 105 K for 33 mJ/cm^2. Furthermore, the mass diffusion limitation is stronger in the Ag NP seeding case, due to a large number of photogenerated valence electrons, a lower ion concentration and a higher pulse repetition rate. This leads to a larger number of excess charge carriers with a limited diffusion length in the TiO_2 film resulting in further temperature increase and a stronger influence of the laser fluence on the Ag NP seeding rate. These temperature considerations can explain some deviation from the unidirectional process response evident from the center point positions in the Ag and Au NP seeding experiments (*level 0*, Fig. 3(b, d)).

The results of the factorial experiment are summarized in Table 2. For the Ag NP seeding, the increase in the laser fluence F_L (A) and ion concentration C_P (B) led to the increase in the seeding rate, hence the increase in the NP deposition density (n_{NP}). The lowest and highest NP densities of 152 and 1070 μm^{-2} were achieved for the lowest and highest A and B parameter combinations, corresponding to the *levels −1* and *1* respectively (see Table 2). The obtained mean centroid distances (d_m) varied from 48 ± 19 nm to 22 ± 5 nm for the low and high n_{NP}

Optical Materials EXPRESS

respectively with a corresponding averaged center point (*levels 0,* Table 2) distance of 34 ± 11 nm. The mean Ag seed diameters (D_m) varied only slightly from 14 ± 9 to 18 ± 5 nm for the lowest and highest parameter combinations respectively.

Table 2. Results of the 2^k factorial experiment for Ag and Au NP seeding

Levels			**Ag**			**Au**		
A	*B*	*C*	D_m *(nm)*	d_m *(nm)*	n_{NP} (μm^{-2})	D_m *(nm)*	d_m *(nm)*	n_{NP} (μm^{-2})
−1	*−1*	*−1*	14 ± 9	48 ± 19	152	16 ± 5	41 ± 15	181
1	*−1*	*−1*	14 ± 4	25 ± 7	708	16 ± 5	30 ± 10	409
−1	*1*	*−1*	16 ± 6	40 ± 15	220	23 ± 6	63 ± 30	69
1	*1*	*−1*	16 ± 6	23 ± 6	907	28 ± 9	47 ± 17	164
−1	*−1*	*1*	15 ± 4	46 ± 18	156	17 ± 5	38 ± 15	212
1	*−1*	*1*	18 ± 5	31 ± 9	369	16 ± 5	28 ± 8	506
−1	*1*	*1*	16 ± 5	37 ± 12	257	26 ± 7	61 ± 26	83
1	*1*	*1*	16 ± 5	22 ± 5	1070	24 ± 8	38 ± 13	239
0	*0*	*0*	15 ± 5	34 ± 11	335	24 ± 7	49 ± 20	134

A different parameter combination leading to the high- and low-density NP coverage was observed in the Au NP seeding experiment. The lowest n_{NP} of 69 μm^{-2}, corresponding to d_m of 63 ± 30 nm, was found for the combination of low laser fluence (A *level −1,* Table 2) and high ion concentration (B *level 1,* Table 2). The highest Au NP density of 506 μm^{-2}, with d_m of 28 ± 8 nm, was observed for the high laser fluence (A *level 1,* Table 2) and low ion concentration (B *level −1,* Table 2). The mean Au seed diameters appeared to be influenced by the initial ion concentration varying from a minimum value of 16 ± 5 nm at 2 mM (*level −1*) to a maximum of 28 ± 9 nm at 8 mM (*level 1*). The observed differences in the Ag and Au seeding behavior can be explained by dynamic coalescence of NPs during early stages of the Au seeding and before the critical particle size is reached which inhibits the surface diffusion and Ostwald ripening [75]. Both dynamic effects are common for small NP with decreased particle-substrate adhesion and increased temperature [75]. Furthermore, the reported exothermic nature of migration coalescence [76] facilitates an autocatalytic effect leading to further coalescence. Recent studies confirmed that the higher activation energy is required for migration of Ag atoms compared to Au atoms on the TiO_2 surface due to lower Au bonding energy at the preferred metal binding sites on TiO_2 [77]. It has to be noted that for the chosen irradiation parameters in the Ag and Au NP seeding study the effect of static coalescence was not observed.

2. NP growth: The optimization towards the smallest interparticle distance was conducted by varying the applied number of pulses per spot (N_L), as this stage is known to be dominated by so-called antenna effect leading to preferential ion reduction on the already deposited NP [30,31]. Based on the results of the factorial experiment, different parameter combinations were used for Ag and Au NP growth with the aim to achieve varying NP densities, thus exploring the possibility to manipulate the NP sizes at short interparticle distances.

The Ag NP growth study was conducted using 3-mM $AgNO_3$ precursor solution containing 10 vol-% of MeOH, consistent with the *level 1* concentrations used in the seeding experiment (Table 1, factors *B* and *C*). Since the laser fluence (F_L) had the largest impact on the particle density, the growth phase was carried out using a set of F_L in the range from 13 and 38 mJ/cm^2 with N_L varied from 1625 to 13047 (see Table 1: *NP growth*). The results of the Ag NP growth are summarized in Table 3. Figure 4(a) and 4(b) show somewhat limited Ag NP growth at F_L = 13 mJ/cm^2 for the N_L range from 1625 to 8784 pulses delivered to the TiO_2 surface in a continuous manner. Considerable acceleration in the NP growth was observed for the N_L range from 8784 to 13047 pulses (Fig. 4(a, b), Table 3), delivered in discrete reirradiation steps of 203 pulses/spot.

Optical Materials EXPRESS

The observed growth dynamics is associated with the depletion of the precursor at the TiO_2 film surface during continuous pulse deposition, leading to a slow, mass-transfer-limited NP growth, whereas the step-like reirradiation enables diffusive re-equilibration of the depleted layer, resulting in the increased NP growth rate. A significant increase in n_{NP} observed in the N_L range from 8784 to 9596 pulses/spot suggests that additional NP seeding events are also taking place. For N_L >10611 pulses/spot, the onset of static coalescence may also contribute to the observed increase in the Ag NP size as the growth is accompanied by small increase in d_m and decrease in n_{NP} (see Fig. 4(a), Table 3). A sharp increase of ~17% in the NP surface coverage was observed in the N_L range from 8784 to 10611 pulses/spot (see Table 3). However, at longer illumination times, N_L > 10611 pulses/spot, the rate of surface coverage appears to decrease which can be associated with radiation shielding of the TiO_2 surface by the already deposited NP [28].

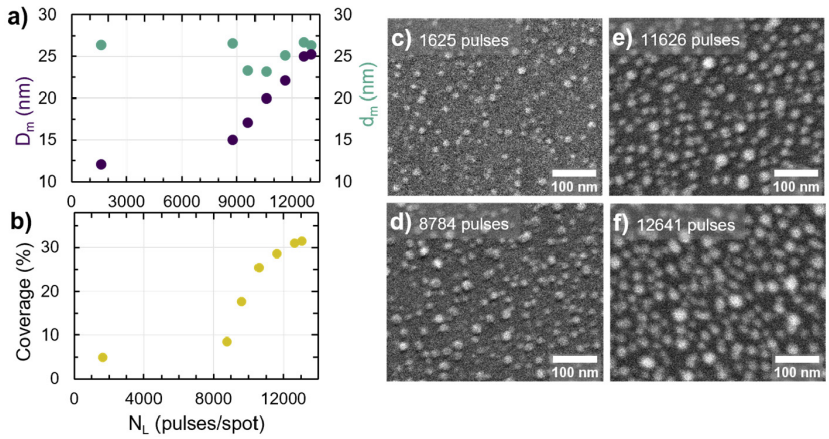

Fig. 4. Regular photocatalytic growth of Ag NPs for $C_P = 3$ mM, $C_S = 10$ vol-%, $F_L = 13$ mJ/cm^2. Evolution of the mean NP diameter (D_m) and centroid distance (d_m) **(a)**, and surface coverage **(b)** with increase in the number of pulses per spot (N_L) from 1625 to 13047. SEM images of the Ag NPs deposited at different N_L **(c - f)**.

The Ag NP growth at higher laser fluences (i.e. F_L >13 mJ/cm^2) led to formation of larger NPs with the surface coverage reaching 55% at $F_L = 38$ mJ/cm^2, $N_L = 8784$ pulses/ spot (see Fig. 5(a); Table 3: *Dewetted NP growth*). The spheroidal shape of the Ag deposits, shown in Fig. 5(b-d), suggests that the NP growth was influenced by melting of the deposited NP followed by coalescence and re-solidification [78]. This process is similar to the thermal dewetting of thin metal films [79], which relies on the minimization of Gibbs free energy to form nano-islands at elevated temperatures, governed by surface-limited diffusion [78]. Unlike conventional dewetting methods, requiring sequential heating with additional metal film deposition in order to achieve high NP density [80], the laser-assisted photodeposition combined with dewetting does not require intermediate metal deposition steps as the photoinduced metal reduction continues while the NP are being dewetted. Moreover, this combined process appears to negate the radiation shielding effect, observed during the low laser fluence growth (Table 3: *NP growth*), allowing for further nanostructure refinement towards high SERS EFs.

The Au NP growth was performed using 2- and 8-mM $HAuCl_4$ precursor solutions containing 20 vol-% of MeOH at 36 and 20 mJ/cm^2 respectively to facilitate a wide range of the resulting NP sizes and densities. The total N_L was varied from 975 to 8970 pulses/spot in successive reirradiations steps of 203 pulses/spot to prevent mass transfer limited growth. The results of Au NP growth are shown in Fig. 6 and are summarized in Table 4. A rapid increase in the NP

Optical Materials EXPRESS

Table 3. Results of the Ag NP growth experiment (C_P = 3 mM, C_S = 10 vol-%)

	D_m (nm)	d_m (nm)	n_{NP} (μm^{-2})	*Coverage* (%)
Regular NP growth				
N_L (pulses/spot)		F_L = *13 mJ/cm*^{2}		
1625	12 ± 3	26 ± 7	608	4.97
8784	15 ± 6	27 ± 7	642	8.54
9596	17 ± 6	23 ± 5	1039	17.61
10611	20 ± 6	23 ± 5	1005	25.42
11626	22 ± 6	25 ± 5	979	28.56
12641	25 ± 9	27 ± 5	842	30.95
13047	25 ± 10	26 ± 5	886	31.5
Dewetted NP growth				
F_L (mJ/cm^2)		N_L = *8784 pulses/spot*		
27.5	31 ± 13	30 ± 6	665	39.51
33	46 ± 19	42 ± 8	354	50.14
38	49 ± 19	43 ± 8	337	54.96

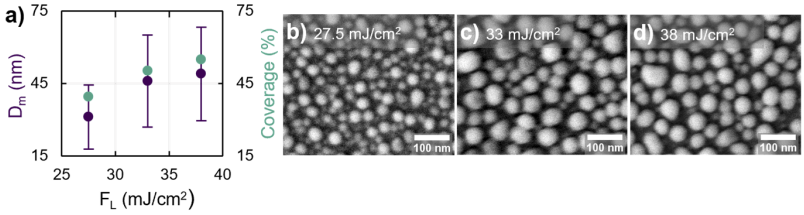

Fig. 5. Dewetted growth of Ag NPs (C_P = 3 mM, C_S = 10 vol%, N_L = 8784 pulses/spot). Evolution of the mean NP diameter (D_m) and NP surface coverage **(a)** is for the laser fluence (F_L) ranging from 27.5 to 38 mJ/cm^2. Corresponding SEM images of the NP **(b-d)**.

density at almost constant NP size was observed at the initial stages of Au growth at N_L = 975 and 1560 pulses/spot with C_P = 2 mM (see Fig. 6(a, b)), suggesting that NP nucleation is still taking place at low NP surface coverage levels, as was also observed during the Ag NP growth. The highest n_{NP} of 599 μm^{-2} with the lowest d_m was found after 1560 pulses/spot (see Table 4: C_P = *2 mM,* F_L = *36 mJ/cm*^{2}). The increase in N_L led to the formation of mainly skewed Au NPs, as seen in Fig. 6(e), and decrease in n_{NP} to 483 μm^{-2} as a result of increasing static coalescence at larger N_L. The rate of surface coverage increased with the number of delivered pulses, reaching a plateau at N_L = 8970 pulses/spot (see Fig. 6(b, e)) due to the onset of radiation shielding. The increase in ion concentration to 8 mM at F_L = 20 mJ/cm^2 led to the deposition of larger NPs at lower density for the same N_L (see Table 4: C_P = *8 mM,* F_L = *20 mJ/cm*^{2}). This is consistent with the dynamic coalescence of Au NPs, also observed in the Au seeding experiment. At N_L = 2145 pulses/spot, formation of Au nanostructures with skewed morphologies was observed (see Fig. 6(f-g)). Further increase in N_L led to formation of the Au films with the surface coverage reaching 95.6% at 9970 pulses/spot (see Fig. 6(h)). Thus, the Au NP growth with high precursor concentrations led to an early onset of static coalescence leading to formation of a peculated film at high N_L. The overall larger standard deviation observed in the Au NP growth study, compared to the Ag growth, are attributed to increased influence of coalescence effects during the Au NP growth.

Optical Materials EXPRESS

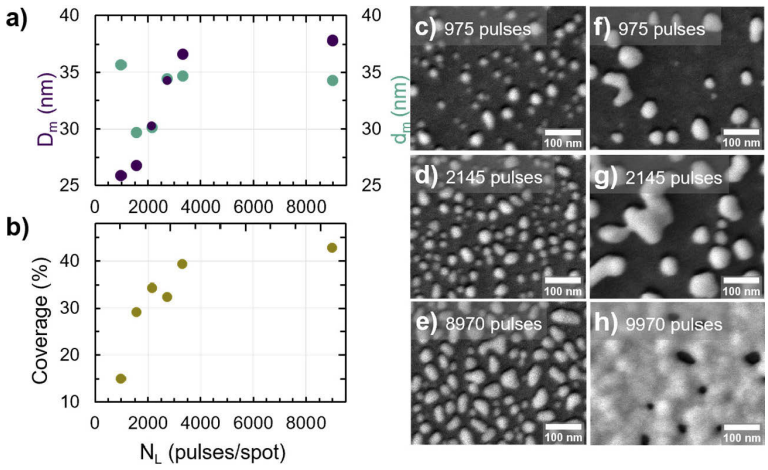

Fig. 6. Au NP growth with $C_P = 2$ mM, $C_S = 20$ vol%, $F_L = 36$ mJ/cm^2 **(a - e)** and $C_P = 8$ mM, $C_S = 20$%, $F_L = 20$ mJ/cm^2 **(f - h)**. Evolution of the mean NP diameter (D_m) and mean centroid distance (d_m) **(a)** and surface coverage **(b)** with increase in the number of pulses per spot (N_L) from 975 to 8970. Corresponding SEM images of the NP **(c-h)**.

Table 4. Results of the Au NP growth experiment (C_S = 20 vol-%)

N_L (pulses/spot)	D_m (nm)	d_m (nm)	n_{NP} (μm^{-2})	*Coverage* (%)
		$C_P = 2$ *mM*, $F_L = 36$ *mJ/cm*^{2}		
975	26 ± 11	36 ± 10	340	14.99
1560	27 ± 14	30 ± 7	599	29.12
2145	30 ± 12	30 ± 6	584	34.30
2730	34 ± 13	34 ± 6	453	32.39
3315	37 ± 18	35 ± 8	456	39.36
8970	38 ± 17	34 ± 7	483	42.85
		$C_P = 8$ *mM*, $F_L = 20$ *mJ/cm*^{2}		
975	48 ± 23	61 ± 19	119	18.86
1170	51 ± 24	61 ± 17	116	20.37
1560	60 ± 26	63 ± 19	111	25.36
2145	81 ± 49	73 ± 23	88	38.86
8970		*film formation*		79.98
9970		*film formation*		95.59

Optical Materials EXPRESS

SERS performance study: The photodeposited Ag and Au nanostructures examined in the SERS study were selected based on previously described criteria for high SERS EF performance. The photodeposition process parameters and SERS performance results are summarized in Table 5. The extinction spectra of the Ag NP used in the study are shown in Fig. 7(a, b). Both sets of spectra for the regular photoinduced (Fig. 7(a)) and combined with dewetting (Fig. 7(b)) Ag NP growth show presence of two extinction bands peaked at ~387 nm and ~520 nm. The long-wavelength band (λ_{SPR2}) can be clearly attributed to the surface plasmon resonance (SPR) of the Ag NPs on TiO_2 surface. The red shift of the SPR band (see Table 5: *Regular NP growth*, λ_{SPR2}) observed on increase of the number of pulses per spot (N_L) was ascribed to the increase in the mean NP size [81,82]. The dewetted NP growth mode (see Table 5: *Dewetted NP growth*, λ_{SPR2}) resulted in the SPR band broadening with a negligible spectral shift of the peak (see Fig. 7(b)). Maxwell-Garnett theory suggests that the SPR broadening is the result of an increase in the mean NP size and increase in the volume filling factor or surface coverage of the Ag NP [83]. The additional short-wavelength band (λ_{SPR1}) was previously observed in the similar Ag - TiO_2 SERS systems [11,19,25], and was attributed to the absorption either due to the presence of small NPs [11] or trapped holes in the TiO_2 film [84]. However, the observed spectral position of the peak and bandwidth of the measured λ_{SPR1} band (Fig. 7(a, b)) as well as the spectral shift of λ_{SPR1} peak with increase in N_L appear to support neither hypotheses. Thus, it can be concluded that λ_{SPR1} band originates from the hybridization effect between the dielectric TiO_2 film and NPs [49]. The asymmetry of dielectric environment at the air/film interface leads to the emergence of additional plasmonic modes normal and parallel to the interface which were shown to be increasingly prominent with increasing film refractive index [85]. Consistent with the hybridization model, these multipolar modes at a planar interface arise from changes to the effective field experienced by the NP due to the reflected and scattered fields at the interface, influenced by the substrate/medium refractive index ratio and NP size [25,86].

Table 5. Results of the SERS performance study

N_L (pulses/spot) / F_L (mJ/cm^2)	λ_{SPR1} (nm)	λ_{SPR2} (nm)	EF_{532} (%RSD)	EF_{633} (%RSD)	EF_{785} (%RSD)
	***Ag NP**: C_P = 3 mM, C_S = 10 vol-%*				
	Regular NP growth				
11626 / 13	383	515	8.30E+04 (8.45%)	5.09E+04 (14.72%)	–
12235 / 13	386	518	9.20E+04 (5.17%)	5.17E+04 (16.29%)	–
12641 / 13	388	523	1.01E+05 (16.38%)	4.68E+04 (15.26%)	–
	Dewetted NP growth				
8784 / 27.5	392	528	1.36E+05 (6.3%)	1.52E+05 (20.67%)	–
8784 / 33	395	527	1.56E+05 (21.2%)	2.73E+05 (28.8%)	1.10E+05 (22.24%)
8784 / 38	391	518	1.36E+05 (9.52%)	5.37E+05 (27.81%)	1.68E+05 (20.69%)
	***Au NP**: C_P = 2 mM, C_S = 20 vol-%*				
2145 / 36	391	540	–	8.52E+04 (10.7%)	–
2730 / 36	394	549	–	9.60E+04 (7.92%)	–
3315 / 36	395	552	–	1.50E+05 (6.4%)	–
8970 / 36	398	547	–	1.26E+05 (19.52%)	–

The Raman spectra of the pure and Ag NP-adsorbed thiophenol used in calculation of the EF are shown in Fig. 7(c). It has to be noted that all SERS measurements were taken in the center of the laser-deposited lines as gaussian intensity distribution of the laser source induces transversal inhomogeneity in the NP deposits, resulting in the decreased EFs towards the edges the laser-written line, as shown for the 785-nm excitation in Fig. 7(d, e). The SERS EF performance of

Optical Materials EXPRESS

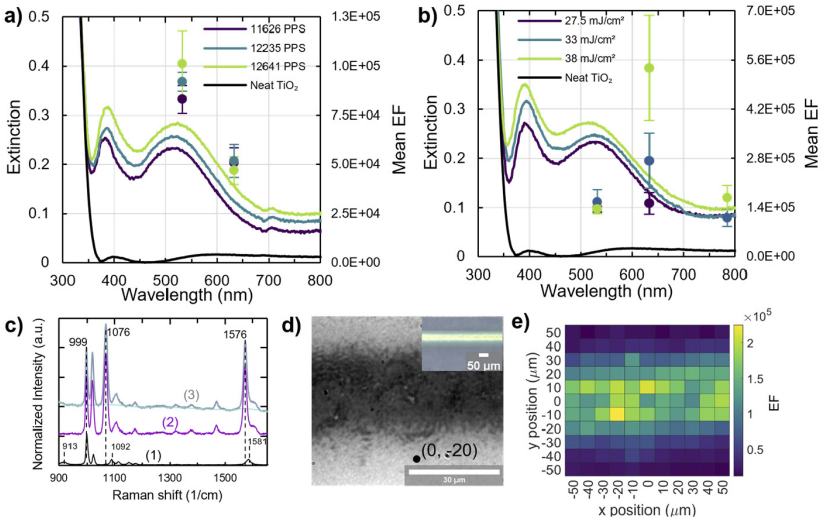

Fig. 7. Extinction spectra and calculated EF with RSD of regularly grown **(a)** and dewetted **(b)** Ag NPs. **(c)** Representative Raman spectra used the EF calculations: 1) Pure thiophenol reference spectrum; 2) SERS spectrum of thiophenol at $\lambda_{exc} = 633$ nm after background correction; 3) SERS spectrum without background correction with the calculated background shown in blue. **(d)** Microscope image of the Ag laser deposition at $F_L = 38$ mJ/cm^2 under 100x magnification. **(e)** 100×100 µm^2 SERS signal mapping of **(d)** at $\lambda_{exc} = 785$ nm with a 10-µm step size with. The black dot in **(d)** corresponds to (0, −20) µm position coordinate in **(e)**.

the regularly grown Ag NPs is shown in Fig. 7(a) and is listed in Table 5. The signal enhancement was observed at 532 and 633 nm excitation which coincides with the long-wavelength shoulder of the λ_{SPR2} band, with the highest EF of 1.01×10^5 achieved for $N_L = 12641$ pulses/spot at $\lambda_{exc} = 532$ nm. A decrease in the EF accompanied by an increase in the relative standard deviation (RSD) of the 1070 cm^{-1} band integrated intensity (*n=21*) was found further away from the maximum of the λ_{SPR2} band at $\lambda_{exc} = 633$ nm. The observed RSD for all regularly grown Ag NP substrates was in the range from 5.2 to 16.4%. No SERS signal was observed at $\lambda_{exc} = 785$ nm. The dewetted Ag NP growth resulted in a superior SERS performance at all *three* excitation wavelengths, with the highest mean EF reaching 5.37×10^5 for $F_L = 38$ mJ/cm^2 at $\lambda_{exc} = 633$ nm (see Fig. 7(b), Table 5: *Dewetted NP growth*). Compared to the regular growth, these Ag NPs had a larger mean diameter as well as higher surface coverage (see Table 3), resulting in the SPR band broadening and larger scattering cross section [87]. The increase in the RSD correlates with the increase in the NP size distribution for the dewetted growth mode (see Table 3: *Dewetted NP growth*).

The extinction spectra of the Au NP are shown in Fig. 8(a). A similar long-wavelength shift of the λ_{SPR2} band (see Table 5) associated with an increase in the mean NP size was observed with increase in N_L. The SERS performance of the Au NP substrates was limited to the 633 nm excitation; no SERS signal was observed at 532 and 785 nm excitations. The increase in Au EFs with the number of deposited pulsed followed the general trend observed for the Ag NPs, with the highest EF reaching 1.5×10^5 (RSD = 6.9%) for $N_L = 3315$ pulses/spot and $F_L = 36$ mJ/cm^2 (Fig. 8(b)). At $N_L = 8970$ pulses/spot, a small reduction in EF accompanied by a substantial RSD increase to ~20% was associated with the skewed Au NP shapes resulting from coalescence as shown in Fig. 6(e).

Optical Materials EXPRESS

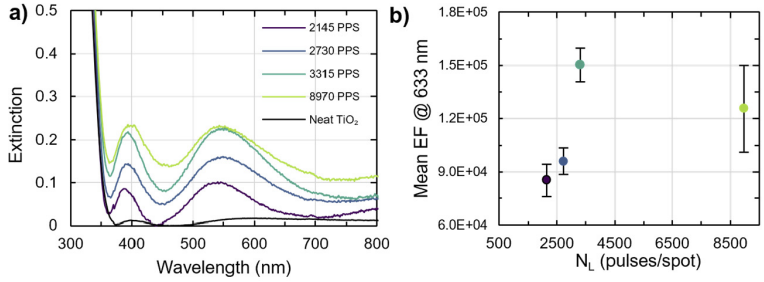

Fig. 8. Extinction spectra **(a)** and corresponding mean SERS EF at 633 nm **(b)** achieved on Au NPs ($C_P = 2$ mM, $C_S = 20$ vol%, $F_L = 36$ mJ/cm^2) deposited at increasing number of pulses per spot (N_L).

Thus, the SERS study showed the optimized photodeposition parameter set for high EF with the Ag-TiO_2 composite substrates should target *growth of larger NP in the 10 - 100 nm diameter range at short interparticle distances below 10 nm*, as seen from Table 3 and 5 for the regularly grown Ag NPs at $\lambda_{exc} = 532$ nm. This was further confirmed by the high SERS EF performance achieved with the dewetted Ag NPs ($D_m > 30$ nm) at all *three* excitation wavelengths (see Table 5: *Dewetted NP growth*). Here, the high levels of $C_p = 3$ mM and $F_L = 38$ mJ/cm^2 at $N_L = 8784$ pulses/spot and $C_s = 10$ vol-% ensured sufficient thermalization and deposition rate for the dewetted NP growth mode. The trends observed in the factorial experiment demonstrate that lower NP densities, thus larger D_m before reaching static coalescence, can be targeted by decreasing C_p and F_L in the regular NP growth. For the dewetted growth case, D_m can be further increased with increase in F_L at otherwise constant parameters. The trend towards larger NP at short interparticle distances for high SERS EF remains true for the Au NP photodeposition, however the influence of dynamic coalescence on final surface morphology has to be taken into account. Here, the high deposition rate at reduced dynamic coalescence was observed for the Au-TiO_2 substrates produced with $C_p = 2$ mM and $F_L = 36$ mJ/cm^2 at $N_L = 2145$ - 8970 pulses/spot and $C_s = 20$ vol-%. At $C_P = 8$ mM, strong influence of dynamic coalescence led to the skewed NP shapes and reduced surface coverage (see Table 4: $C_P = 8$ *mM,* $F_L = 20$ *mJ/cm*^{2}). Therefore, the Au NP with $D_m > 30$ nm can be achieved by a small increase in C_P, below 8 mM.

Typically reported SERS EF values of the photodeposited Ag-TiO_2 composite substrates are in the range from 10^5 to 10^6 [21,22,25] for λ_{exc} in the range from 514 to 532 nm. The highest EF value of 1.2×10^6 was reported for 4-MBA probe molecules under nonresonant excitation [25]. Despite similarities between the nanostructures, the EFs achieved in this work are on average one order of magnitude smaller than reported in Ref. [25]. This can be attributed to a strong binding affinity of 4-MBA to TiO_2 [88] which leads to an additional increase in the EF value due to the charge-transfer-induced SERS through electron injection from the TiO_2 conduction band to the surface bonded molecules [13]. The opposing EF trends with increase in D_m observed in Ref. [25] can be attributed to the NP size dependent charge transfer kinetics [89]. The SERS performance of the Au nanostructures produced in this work appears to surpass the values reported earlier for the Au-TiO_2 systems. The EF values of similar substrates range from 7×10^3 [14] to 7×10^4 [26] at $\lambda_{exc} = 633$ nm using 4-MBA as a probe molecule. Herein the higher surface coverage with larger Au NP enabled further improvement of the SERS performance with the EF reaching 1.5×10^5 with thiophenol probe. Admittedly the EF values of the photodeposited SERS platforms are still short of those achieved by other established methods such as nanosphere lithography with SERS EFs of $\sim 10^8$ for the substrate matched λ_{exc} [45]. However, the simplicity and scalability of the photocatalytic production method is increasingly recognized as a prerequisite for translating SERS platforms to practical analytical applications.

Optical Materials EXPRESS

Further increase in the SERS EF performance, beyond the 10^5 mark, can be achieved for the SERS composite platforms with larger NP sizes at high surface coverages (e.g. for the Ag-TiO_2 composite substrate, D_m > 50 nm at surface coverage > 55% should be attained). This can be realised in the Ag-TiO_2 systems via the dewetted growth mode. The regular growth mode at the precursor concentrations below 8 mM can be employed for the Au-TiO_2 systems at low NP seeding densities. For the probe molecules benefiting from the charge-transfer effect (e.g. 4-MBA), smaller D_m at higher NP seeding densities are required to achieve large charge-transfer contributed SERS EFs. The self-cleaning performance of the Ag/Au-TiO_2 substrate will be studied in our future works as a route towards recyclable SERS platforms.

4. Conclusion

The ns-pulsed laser-assisted photocatalytic growth optimization procedure based on the design of experiment approach is demonstrated by monitoring single and combined influences of the laser fluence, number of pulses per spot, precursor and sacrificial agent concentrations. The TiO_2 film properties were independently optimized to achieve highly localized photodeposition. It was found that the Ag and Au NP seeding rates increase with increase in the laser fluence and metal ion concentration in a mass-transport-limited process. The increase in the sacrificial agent concentrations had little to no effect on the NP deposition rate. However, the initial screening experiments showed that the process is significantly slowed down if no sacrificial agent was added. In the case of Au NP seeding, the metal ion concentrations above 2 mM led to increase in surface migration and dynamic coalescence resulting in decrease in Au NP seeding density. In contrast, the Ag NP seeding density increased with increase in the precursor concentration. The NP growth mode was supported by the increasing in the number of delivered pulses per spot. Some additional NP seeding during the growth was noted, particularly when the step reirradiation was applied. The examined processes were additionally influenced by the laser induced heating. At high laser fluences, the laser induced heating enable a different NP growth mode accompanied by NP melting, coalescence and re-solidification. This resulted in a larger mean NP size as well as higher surface coverage thus circumventing the problem of static coalescence occurring during the regular photocatalytic growth. The SERS performance study conducted at 532, 633 and 785 nm showed that the high enhancement SERS nanostructures can be reliably achieved by controlling a small number of the film-independent parameters. Considering the conservative approach used in the SERS EF calculation, the values presented here provide a meaningful baseline for the EFs achievable with photodeposited SERS platforms.

Funding. Engineering and Physical Sciences Research Council (EP/P008135/2, EP/S017445/1).

Acknowledgments. The authors acknowledge support from EPSRC through EP/P008135/2 and EP/S017445/1.

Disclosures. The authors declare no conflicts of interest.

Data availability. Data underlying the results presented in this paper are available in Ref. [90].

References

1. K. Kneipp, Y. Wang, H. Kneipp, L. T. Perelman, I. Itzkan, R. R. Dasari, and M. S. Feld, "Single molecule detection using surface-enhanced Raman scattering (SERS)," Phys. Rev. Lett. **78**(9), 1667–1670 (1997).
2. S. Nie and S. R. Emory, "Probing single molecules and single nanoparticles by surface-enhanced Raman scattering," Science **275**(5303), 1102–1106 (1997).
3. S. McAughtrie, K. Faulds, and D. Graham, "Surface enhanced Raman spectroscopy (SERS): Potential applications for disease detection and treatment," J. Photochem. Photobiol., C **21**, 40–53 (2014).
4. X. Qian, X.-H. Peng, D. O. Ansari, Q. Yin-Goen, G. Z. Chen, D. M. Shin, L. Yang, A. N. Young, M. D. Wang, and S. Nie, "In vivo tumor targeting and spectroscopic detection with surface-enhanced Raman nanoparticle tags," Nat. Biotechnol. **26**(1), 83–90 (2008).
5. O. Lyandres, N. C. Shah, C. R. Yonzon, J. T. Walsh, M. R. Glucksberg, and R. P. van Duyne, "Real-time glucose sensing by surface-enhanced Raman spectroscopy in bovine plasma facilitated by a mixed decanethiol/mercaptohexanol partition layer," Anal. Chem. **77**(19), 6134–6139 (2005).

Optical Materials EXPRESS

6. R. M. Jarvis and R. Goodacre, "Discrimination of bacteria using surface-enhanced Raman spectroscopy," Anal. Chem. **76**(1), 40–47 (2004).
7. M. Fan, G. F. S. Andrade, and A. G. Brolo, "A review on the fabrication of substrates for surface enhanced Raman spectroscopy and their applications in analytical chemistry," Anal. Chim. Acta **693**(1-2), 7–25 (2011).
8. S. Schlücker, "Surface-enhanced Raman spectroscopy: concepts and chemical applications," Angew. Chem. **53**(19), 4756–4795 (2014).
9. A. Shiohara, Y. Wang, and L. M. Liz-Marzán, "Recent approaches toward creation of hot spots for SERS detection," J. Photochem. Photobiol., C **21**, 2–25 (2014).
10. F. Akbarian, B. S. Dunn, and J. I. Zink, "Surface-enhanced raman spectroscopy using photodeposited gold particles in porous sol-gel silicates," J. Phys. Chem. **99**(12), 3892–3894 (1995).
11. A. Mills, G. Hill, M. Stewart, D. Graham, W. E. Smith, S. Hodgen, P. J. Halfpenny, K. Faulds, and P. Robertson, "Characterization of novel Ag on TiO_2 films for surface-enhanced Raman scattering," Appl. Spectrosc. **58**(8), 922–928 (2004).
12. S. Fateixa, H. I. S. Nogueira, and T. Trindade, "Hybrid nanostructures for SERS: materials development and chemical detection," Phys. Chem. Chem. Phys. **17**(33), 21046–21071 (2015).
13. L. Yang, X. Jiang, W. Ruan, J. Yang, B. Zhao, W. Xu, and J. R. Lombardi, "Charge-transfer-induced surface-enhanced Raman scattering on Ag–TiO_2 nanocomposites," J. Phys. Chem. C **113**(36), 16226–16231 (2009).
14. X. Jiang, X. Sun, D. Yin, X. Li, M. Yang, X. Han, L. Yang, and B. Zhao, "Recyclable Au-TiO_2 nanocomposite SERS-active substrates contributed by synergistic charge-transfer effect," Phys. Chem. Chem. Phys. **19**(18), 11212–11219 (2017).
15. Q. Huang, J. Li, W. Wei, Y. Wu, and T. Li, "Synthesis, characterization and application of TiO_2/Ag recyclable SERS substrates," RSC Adv. **7**(43), 26704–26709 (2017).
16. X. Li, G. Chen, L. Yang, Z. Jin, and J. Liu, "Multifunctional Au-coated TiO_2 Nanotube arrays as recyclable SERS substrates for multifold organic pollutants detection," Adv. Funct. Mater. **20**(17), 2815–2824 (2010).
17. Y. Zhao, L. Sun, M. Xi, Q. Feng, C. Jiang, and H. Fong, "Electrospun TiO_2 nanofelt surface-decorated with Ag nanoparticles as sensitive and UV-cleanable substrate for surface enhanced Raman scattering," ACS Appl. Mater. Interfaces **6**(8), 5759–5767 (2014).
18. A. Wolosiuk, N. G. Tognalli, E. D. Martínez, M. Granada, M. C. Fuertes, H. Troiani, S. A. Bilmes, A. Fainstein, and G. J. A. A. Soler-Illia, "Silver nanoparticle-mesoporous oxide nanocomposite thin films: a platform for spatially homogeneous SERS-active substrates with enhanced stability," ACS Appl. Mater. Interfaces **6**(7), 5263–5272 (2014).
19. S. Li, Q. Tao, D.-W. Li, K. Liu, and Q.-Y. Zhang, "Photocatalytic growth and plasmonic properties of Ag nanoparticles on TiO_2 films," J. Mater. Res. **30**(2), 304–314 (2015).
20. Í. A. Costa, A. P. Maciel, M. J. A. Sales, S. G. C. Moreira, and L. G. Paterno, "The role played by graphene oxide in the photodeposition and surface-enhanced raman scattering activity of plasmonic Ag nanoparticle substrates," Phys. Status Solidi A **217**(5), 1900965 (2020).
21. T.-L. Guo, J.-G. Li, D.-H. Ping, X. Sun, and Y. Sakka, "Controlled photocatalytic growth of Ag nanocrystals on brookite and rutile and their SERS performance," ACS Appl. Mater. Interfaces **6**(1), 236–243 (2014).
22. L. He, D. Riassetto, P. Bouvier, L. Rapenne, O. Chaix-Pluchery, V. Stambouli, and M. Langlet, "Controlled growth of silver nanoparticles through a chemically assisted photocatalytic reduction process for SERS substrate applications," J. Photochem. Photobiol., A **277**, 1–11 (2014).
23. Q. Huang, S. Liu, W. Wei, Q. Yan, and C. Wu, "Selective synthesis of different ZnO/Ag nanocomposites as surface enhanced Raman scattering substrates and highly efficient photocatalytic catalysts," RSC Adv. **5**(34), 27075–27081 (2015).
24. X. Dou, X. Li, L. Qin, S. Han, and S.-Z. Kang, "An ultrasensitive, disposable, and "plug and play" surface-enhanced raman scattering substrate for the in situ detection of trace thiram in water," ACS Appl. Nano Mater. **1**(9), 4955–4963 (2018).
25. E. Wiercigroch, A. Kisielewska, A. Blat, A. Wislocka, I. Piwoński, and K. Malek, "Photocatalytical decoration of thin titania coatings with silver nanostructures provides a robust and reproducible SERS signal," J. Raman Spectrosc. **50**(11), 1649–1660 (2019).
26. E. Wiercigroch, P. Swit, A. Kisielewska, I. Piwoński, and K. Malek, "Photocatalytic deposition of plasmonic Au nanostructures on a semiconductor substrate to enhance Raman sensitivity," Appl. Surf. Sci. **529**, 147021 (2020).
27. A. Fujishima, X. Zhang, and D. Tryk, "TiO_2 photocatalysis and related surface phenomena," Surf. Sci. Rep. **63**(12), 515–582 (2008).
28. K. Wenderich and G. Mul, "Methods, mechanism, and applications of photodeposition in photocatalysis. a review," Chem. Rev. **116**(23), 14587–14619 (2016).
29. E. Barnes, L. Soblosky, E. M. Alberts, L. Johnson, J. G. M. Guy, and A. Kumar, "Photochemically patterned metal nanoparticle strontium barium niobate surfaces with tunable wettability, enhanced Raman scattering, and fluorescence emission," Appl. Phys. Lett. **115**(1), 011601 (2019).
30. D. Friedmann, H. Hansing, and D. Bahnemann, "Primary processes during the photodeposition of Ag clusters on TiO_2 nanoparticles," Z. Phys. Chem. **221**(3), 329–348 (2007).
31. A. Fernandez, A. Caballero, A. R. Gonzalez-Elipe, J.-M. Herrmann, H. Dexpert, and F. Villain, "In Situ EXAFS study of the photocatalytic reduction and deposition of gold on colloidal titania," J. Phys. Chem. **99**(10), 3303–3309 (1995).

Optical Materials EXPRESS

32. H.-J. Nam, T. Amemiya, M. Murabayashi, and K. Itoh, "Photocatalytic activity of Sol–Gel TiO_2 thin films on various kinds of glass substrates: the effects of Na+ and primary particle size," J. Phys. Chem. B **108**(24), 8254–8259 (2004).
33. J. Krýsa, P. Novotná, Š. Kment, and A. Mills, "Effect of glass substrate and deposition technique on the properties of sol gel TiO_2 thin films," J. Photochem. Photobiol., A **222**(1), 81–86 (2011).
34. S. C. Chan and M. A. Barteau, "Preparation of highly uniform Ag/TiO_2 and Au/TiO_2 supported nanoparticle catalysts by photodeposition," Langmuir **21**(12), 5588–5595 (2005).
35. Z. Starowicz, M. Lipiński, R. P. Socha, K. Berent, G. Kulesza, and P. Ozga, "Photochemical silver nanoparticles deposition on sol–gel TiO_2 for plasmonic properties utilization," J. Sol-Gel Sci. Technol. **73**(3), 563–571 (2015).
36. C. Tossi, L. Hällström, J. Selin, M. Vaelma, E. See, J. Lahtinen, and I. Tittonen, "Size- and density-controlled photodeposition of metallic platinum nanoparticles on titanium dioxide for photocatalytic applications," J. Mater. Chem. A **7**(24), 14519–14525 (2019).
37. I. J. Jahn, O. Žukovskaja, X.-S. Zheng, K. Weber, T. W. Bocklitz, D. Cialla-May, and J. Popp, "Surface-enhanced Raman spectroscopy and microfluidic platforms: challenges, solutions and potential applications," Analyst **142**(7), 1022–1047 (2017).
38. N. Negishi, "Preparation of transparent TiO_2 thin film photocatalyst and its photocatalytic activity," Chem. Lett. **24**(9), 841–842 (1995).
39. S. Berg, D. Kutra, T. Kroeger, C. N. Straehle, B. X. Kausler, C. Haubold, M. Schiegg, J. Ales, T. Beier, M. Rudy, K. Eren, J. I. Cervantes, B. Xu, F. Beuttenmueller, A. Wolny, C. Zhang, U. Koethe, F. A. Hamprecht, and A. Kreshuk, "ilastik: interactive machine learning for (bio)image analysis," Nat. Methods **16**(12), 1226–1232 (2019).
40. J. Schindelin, I. Arganda-Carreras, E. Frise, V. Kaynig, M. Longair, T. Pietzsch, S. Preibisch, C. Rueden, S. Saalfeld, B. Schmid, J.-Y. Tinevez, D. J. White, V. Hartenstein, K. Eliceiri, P. Tomancak, and A. Cardona, "Fiji - an Open Source platform for biological image analysis," Nat. Methods **9**(7), 676–682 (2012).
41. H. G. Schulze, R. B. Foist, K. Okuda, A. Ivanov, and R. F. B. Turner, "A small-window moving average-based fully automated baseline estimation method for Raman spectra," Appl. Spectrosc. **66**(7), 757–764 (2012).
42. D. Prezgot and A. Ianoul, "Probing the anisotropy of SERS enhancement with spatially separated plasmonic modes in strongly coupled silver nanocubes on a dielectric substrate," J. Phys. Chem. C **119**(6), 3293–3301 (2015).
43. C. E. Taylor, J. E. Pemberton, G. G. Goodman, and M. H. Schoenfisch, "Surface enhancement factors for Ag and Au surfaces relative to Pt surfaces for monolayers of thiophenol," Appl. Spectrosc. **53**(10), 1212–1221 (1999).
44. E. C. Le Ru, E. Blackie, M. Meyer, and P. G. Etchegoin, "Surface enhanced Raman scattering enhancement factors: a comprehensive study," J. Phys. Chem. C **111**(37), 13794–13803 (2007).
45. C. L. Haynes and R. P. van Duyne, "Plasmon-sampled surface-enhanced Raman excitation spectroscopy," J. Phys. Chem. B **107**(30), 7426–7433 (2003).
46. L. Gunnarsson, E. J. Bjerneld, H. Xu, S. Petronis, B. Kasemo, and M. Käll, "Interparticle coupling effects in nanofabricated substrates for surface-enhanced Raman scattering," Appl. Phys. Lett. **78**(6), 802–804 (2001).
47. Z. Zhu, T. Zhu, and Z. Liu, "Raman scattering enhancement contributed from individual gold nanoparticles and interparticle coupling," Nanotechnology **15**(3), 357–364 (2004).
48. W. Rechberger, A. Hohenau, A. Leitner, J. R. Krenn, B. Lamprecht, and F. R. Aussenegg, "Optical properties of two interacting gold nanoparticles," Opt. Commun. **220**(1-3), 137–141 (2003).
49. E. Prodan, C. Radloff, N. J. Halas, and P. Nordlander, "A hybridization model for the plasmon response of complex nanostructures," Science **302**(5644), 419–422 (2003).
50. H. Xu, J. Aizpurua, M. Kall, and P. Apell, "Electromagnetic contributions to single-molecule sensitivity in surface-enhanced raman scattering," Phys. Rev. E: Stat. Phys., Plasmas, Fluids, Relat. Interdiscip. Top. **62**(3), 4318–4324 (2000).
51. Y. Fujita, R. Aubert, P. Walke, H. Yuan, B. Kenens, T. Inose, C. Steuwe, S. Toyouchi, B. Fortuni, M. Chamtouri, K. P. F. Janssen, S. Feyter, M. B. J. Roeffaers, and H. Uji-i, "Highly controllable direct femtosecond laser writing of gold nanostructures on titanium dioxide surfaces," Nanoscale **9**(35), 13025–13033 (2017).
52. I. Piwoński, K. Kądzioła, A. Kisielewska, K. Soliwoda, M. Wolszczak, K. Lisowska, N. Wrońska, and A. Felczak, "The effect of the deposition parameters on size, distribution and antimicrobial properties of photoinduced silver nanoparticles on titania coatings," Appl. Surf. Sci. **257**(16), 7076–7082 (2011).
53. V. Iliev, D. Tomova, L. Bilyarska, and G. Tyuliev, "Influence of the size of gold nanoparticles deposited on TiO_2 upon the photocatalytic destruction of oxalic acid," J. Mol. Catal. A: Chem. **263**(1-2), 32–38 (2007).
54. J. Ma, S. Guo, X. Guo, and H. Ge, "Modified photodeposition of uniform Ag nanoparticles on TiO_2 with superior catalytic and antibacterial activities," J. Sol-Gel Sci. Technol. **75**(2), 366–373 (2015).
55. D. C. Montgomery, *Design and Analysis of Experiments*, 8th edition (John Wiley & Sons Inc, 2013).
56. I. Piwoński, K. Spilarewicz-Stanek, A. Kisielewska, K. Kądzioła, M. Cichomski, and J. Ginter, "Examination of Ostwald ripening in the photocatalytic growth of silver nanoparticles on titanium dioxide coatings," Appl. Surf. Sci. **373**, 38–44 (2016).
57. R. Memming, *Semiconductor Electrochemistry*, 2nd edition (Wiley-VCH, 2015).
58. M. A. Henderson, "A surface science perspective on TiO_2 photocatalysis," Surf. Sci. Rep. **66**(6-7), 185–297 (2011).
59. P. Docampo, S. Guldin, U. Steiner, and H. J. Snaith, "Charge transport limitations in self-assembled TiO_2 photoanodes for dye-sensitized solar cells," J. Phys. Chem. Lett. **4**(5), 698–703 (2013).

Optical Materials EXPRESS

60. Y. Yu, K. Wu, S. Lu, K. Ma, S. Zhong, H. Zhang, Y. Zhu, J. Guo, H. Yue, C. Liu, S. Tang, and B. Liang, "Engineering an ultrathin amorphous TiO_2 layer for boosting the weatherability of TiO_2 pigment with high lightening power," Chin. J. Chem. Eng. **27**(11), 2825–2834 (2019).
61. M. Shalom, S. Dor, S. Rühle, L. Grinis, and A. Zaban, "Core/CdS quantum dot/shell mesoporous solar cells with improved stability and efficiency using an amorphous TiO_2 coating," J. Phys. Chem. C **113**(9), 3895–3898 (2009).
62. W. F. Zhang, Y. L. He, M. S. Zhang, Z. Yin, and Q. Chen, "Raman scattering study on anatase TiO_2 nanocrystals," J. Phys. D: Appl. Phys. **33**(8), 912–916 (2000).
63. J. Tauc, R. Grigorovici, and A. Vancu, "Optical properties and electronic structure of amorphous germanium," Phys. Status Solidi B **15**(2), 627–637 (1966).
64. M. Cesaria, A. P. Caricato, and M. Martino, "Realistic absorption coefficient of ultrathin films," J. Opt. **14**(10), 105701 (2012).
65. D. Reyes-Coronado, G. Rodríguez-Gattorno, M. E. Espinosa-Pesqueira, C. Cab, C. R. de, and G. Oskam, "Phase-pure TiO_2 nanoparticles: anatase, brookite and rutile," Nanotechnology **19**(14), 145605 (2008).
66. H. K. Pulker, *Coatings on Glass*, 2nd ed., revised (Elsevier Science, 1999).
67. Y. Chimupala, G. Hyett, R. Simpson, R. Mitchell, R. Douthwaite, S. J. Milne, and R. D. Brydson, "Synthesis and characterization of mixed phase anatase TiO_2 and sodium-doped TiO_2(B) thin films by low pressure chemical vapour deposition (LPCVD)," RSC Adv. **4**(89), 48507–48515 (2014).
68. G. A. Tompsett, G. A. Bowmaker, R. P. Cooney, J. B. Metson, K. A. Rodgers, and J. M. Seakins, "The Raman Spectrum of Brookite, TiO_2 (Pbca, 2 = 8)," J. Raman Spectrosc. **26**(1), 57–62 (1995).
69. A. J. Nozik and R. Memming, "Physical chemistry of semiconductor−liquid interfaces," J. Phys. Chem. **100**(31), 13061–13078 (1996).
70. J. Schneider, D. Bahnemann, J. Ye, J. Ye, G. L. Puma, G. L. Puma, and D. D Dionysiou, *Photocatalysis Fundamentals and Applications* (RSC, 2014).
71. L. A. H. Fleming, G. Tang, S. A. Zolotovskaya, and A. Abdolvand, "Controlled modification of optical and structural properties of glass with embedded silver nanoparticles by nanosecond pulsed laser irradiation," Opt. Mater. Express **4**(5), 969 (2014).
72. S. J. Smith, R. Stevens, S. Liu, G. Li, A. Navrotsky, J. Boerio-Goates, and B. F. Woodfield, "Heat capacities and thermodynamic functions of TiO_2 anatase and rutile: Analysis of phase stability," Am. Mineral. **94**(2-3), 236–243 (2009).
73. B. Danielzik, M. Heming, D. Krause, and A. Thelen, *Thin Films on Glass* (Springer-Verlag Berlin, 2003).
74. E. G. Birgin, I. Chambouleyron, and J. M. Martínez, "Estimation of the optical constants and the thickness of thin films using unconstrained optimization," J. Comput. Phys. **151**(2), 862–880 (1999).
75. M. José-Yacaman, C. Gutierrez-Wing, M. Miki, D.-Q. Yang, K. N. Piyakis, and E. Sacher, "Surface diffusion and coalescence of mobile metal nanoparticles," J. Phys. Chem. B **109**(19), 9703–9711 (2005).
76. H. Shirakawa and H. Komiyama, "Migration-coalescence of nanoparticles during deposition of Au, Ag, Cu, and GaAs on Amorphous SiO_2," J. Nanopart. Res. **1**(1), 17–30 (1999).
77. A. Alghannam, C. L. Muhich, and C. B. Musgrave, "Adatom surface diffusion of catalytic metals on the anatase TiO_2(101) surface," Phys. Chem. Chem. Phys. **19**(6), 4541–4552 (2017).
78. S. J. Henley, J. D. Carey, and S. R. P. Silva, "Pulsed-laser-induced nanoscale island formation in thin metal-on-oxide films," Phys. Rev. B **72**(19), 195408 (2005).
79. J. Quan, J. Zhang, X. Qi, J. Li, N. Wang, and Y. Zhu, "A study on the correlation between the dewetting temperature of Ag film and SERS intensity," Sci. Rep. **7**(1), 14771 (2017).
80. M. Kang, S.-G. Park, and K.-H. Jeong, "Repeated solid-state dewetting of thin gold films for nanogap-rich plasmonic nanoislands," Sci. Rep. **5**(1), 14790 (2015).
81. K. L. Kelly, E. Coronado, L. L. Zhao, and G. C. Schatz, "The optical properties of metal nanoparticles: the influence of size, shape, and dielectric environment," J. Phys. Chem. B **107**(3), 668–677 (2003).
82. S. K. Ghosh and T. Pal, "Interparticle coupling effect on the surface plasmon resonance of gold nanoparticles: from theory to applications," Chem. Rev. **107**(11), 4797–4862 (2007).
83. V. M. Shalaev, *Optical Properties of Nanostructured Random Media* (Springer, 2002).
84. D. Bahnemann, A. Henglein, J. Lilie, and L. Spanhel, "Flash photolysis observation of the absorption spectra of trapped positive holes and electrons in colloidal titanium dioxide," J. Phys. Chem. **88**(4), 709–711 (1984).
85. M. W. Knight, Y. Wu, J. B. Lassiter, P. Nordlander, and N. J. Halas, "Substrates matter: influence of an adjacent dielectric on an individual plasmonic nanoparticle," Nano Lett. **9**(5), 2188–2192 (2009).
86. J. Lermé, C. Bonnet, M. Broyer, E. Cottancin, D. Manchon, and M. Pellarin, "Optical properties of a particle above a dielectric interface: cross sections, benchmark calculations, and analysis of the intrinsic substrate effects," J. Phys. Chem. C **117**(12), 6383–6398 (2013).
87. G. Baffou and R. Quidant, "Thermo-plasmonics: using metallic nanostructures as nano-sources of heat," Laser Photonics Rev. **7**(2), 171–187 (2013).
88. L. Yang, X. Jiang, W. Ruan, B. Zhao, W. Xu, and J. R. Lombardi, "Adsorption study of 4-MBA on TiO_2 nanoparticles by surface-enhanced Raman spectroscopy," J. Raman Spectrosc. **40**(12), 2004–2008 (2009).
89. J. Song, J. Long, Y. Liu, Z. Xu, A. Ge, B. D. Piercy, D. A. Cullen, I. N. Ivanov, J. R. McBride, M. D. Losego, and T. Lian, "Highly efficient plasmon induced hot-electron transfer at Ag/TiO_2 Interface," ACS Photonics **8**(5), 1497–1504 (2021).

Optical Materials EXPRESS

90. M. Hoffmann, S. Wackerow, A. Abdolvand, and S. A. Zolotovskaya, "High performance SERS platforms via parametric optimization of laser-assisted photodeposition of silver and gold nanoparticles," SharePoint, 2021, https://dx.doi.org/10.15132/10000168.